

Fabrication of MoS₂@g-C₃N₄ core-shell nanospheres for visible light photocatalytic degradation of toluene

Xin Wang · Wei Xiong · Xinyong Li  · Qidong Zhao · Shiyang Fan · Mingmei Zhang · Jincheng Mu · Aicheng Chen

Received: 27 February 2018 / Accepted: 24 August 2018 / Published online: 10 September 2018
© Springer Nature B.V. 2018

Abstract The semiconductor-based photocatalytic oxidation process is considered as one of the most economical and environmentally friendly approach for the degradation of toluene. For the sake of exploring an efficient visible-light-driven photocatalysts, the MoS₂@g-C₃N₄ core-shell nanospheres were successfully fabricated by taking the advantages of the morphology and structure of materials tailoring and semiconductor coupling, via a two-step approach including the hydrothermal method followed by ultrasonic adhering approach. The morphology, crystallinity, composition, and optical property of as-prepared catalysts were well characterized. The core-shell structure was fabricated by using MoS₂ as the template and the coating of g-C₃N₄ improved the separation of photoinduced charges, due to the strong electronic interaction between them. The photocatalytic activity of MoS₂@g-C₃N₄ core-shell nanospheres had been investigated by the degradation of toluene under visible light irradiation using in situ Fourier transform infrared (FTIR) spectroscopy. The MoS₂@g-C₃N₄ nanospheres displayed enhanced

visible-light photocatalytic activity, which is about 1.3 and 9.6 times than that of g-C₃N₄ and MoS₂ nanospheres under identical conditions. Electron spin resonance (ESR) examinations confirmed the generation of ·OH and ·O₂⁻, which were the key reactive oxygen species involved in the photocatalytic process.

Keywords MoS₂@g-C₃N₄ · Core-shell nanospheres · Visible light photocatalysis · Toluene · Nanostructured catalyst

Introduction

Volatile organic pollutants (VOCs), released from the extensive chemical products, have recently attracted great attention because of their environmental persistence and high toxicity (Aguero et al. 2009; Atkinson and Arey 2003; Kostianen 1995; Sun et al. 2013; Wang et al. 2014b). Toluene, one most typical and ubiquitous hazardous components of VOCs, which is usually found in the exhaust gases from vehicles and indoor air, has severely threatened human health (Liu et al. 2015; Sun et al. 2015). There is an urgent need to develop viable elimination methods towards toluene. For the past decades, a large number of strategies have been reported as potential removal methods for toluene, such as plasma (Mista and Kacprzyk 2008), biodegradation (Malhautier et al. 2014), adsorption (Gil et al. 2014; Puértolas et al. 2014), and catalysis (Kesavan et al. 2011; Sun et al. 2014). Among them, the semiconductor-based photocatalytic oxidation process is considered as one of the

X. Wang · W. Xiong · X. Li (✉) · Q. Zhao · S. Fan · M. Zhang · J. Mu
State Key Laboratory of Fine Chemicals, Key Laboratory of Industrial Ecology and Environmental Engineering (MOE), School of Environmental Science and Technology, Dalian University of Technology, Dalian 116024, China
e-mail: xyli@dlut.edu.cn

X. Li · A. Chen (✉)
Department of Chemistry, University of Guelph, 50 Stone Rd E, Guelph, Ontario N1G 2W1, Canada
e-mail: aicheng@uoguelph.ca

most economical and environmentally friendly approach for the environmental pollutant remediation, due to the huge advantage of strong oxidizing ability, utilization of sunlight, and complete mineralization of organics (Parida et al. 2010; Wang et al. 2010; Yu et al. 2009; Yurdakal et al. 2008; AlShehri et al. 2017a; Ahmad et al. 2017; AlShehri et al. 2017b). In order to improve the utilization of sunlight and enhance the activity for the practical application, a number of attempts have focused on the development of efficient visible-light-driven photocatalysts (Hou et al. 2012; Xiong et al. 2011).

As a member of the layered transition metal dichalcogenides, MoS₂ nanosheets have attracted increasing interest in catalysis, energy storage, electronics, and optoelectronics (Choi et al. 2014; Cummins et al. 2015; Hwang et al. 2011; Lukowski et al. 2013; Yu et al. 2014; Zhou et al. 2013). However, the rapid recombination of photoinduced charges and poor activity limits the practical applications of MoS₂ in the photocatalytic elimination of pollutants. To date, various strategies have been put forward to address these problems. One effective strategy should be the tailor of the nanomaterials to obtain a suitable geometric structure and morphology to provide the effective carrier transfer pathways (Li et al. 2015a; Wang et al. 2013; Wang et al. 2014a). Luo et al. reported the assembling of the MoS₂ nanosheets into a 3D hierarchical architecture (Zhang et al. 2014). By this approach, it can retain the large contact surface and exposes the highly active edge sites for the adsorption of substance and catalysis. Indeed, this solution improves the performance of MoS₂ in lithium storage and hydrogen evolution reaction, and proves promising in photocatalysis. Another one is semiconductor coupling (Barpuzary et al. 2015; Hou et al. 2016; Jiang et al. 2015; Li et al. 2015a; Lu et al. 2016; Zhao et al. 2016). In order to improve the photocatalytic activity of MoS₂, a few recipes have been developed on the coupling with graphitic carbon nitride (g-C₃N₄) (Li et al. 2012), BiVO₄ (Li et al. 2015a), CdS (Chen et al. 2012), CoS₂ (Huang et al. 2015), Fe₃O₄ (Lin et al. 2015), etc. Especially, g-C₃N₄, a typical metal-free polymeric semiconductor material has received great attentions due to its low toxicity and visible light response (Li et al. 2015b). For example, Lu et al. fabricated g-C₃N₄/ultrathin MoS₂ nanosheet hybrid nanostructures with enhanced photocatalytic performance (Lu et al. 2016). Hou et al. reported that MoS₂/g-CN layered junctions were fabricated and used for hydrogen-

evolution catalysis (Hou et al. 2013). Therefore, coupling with g-C₃N₄ makes MoS₂ a potential material for photocatalysis. Nonetheless, 3D MoS₂ hierarchical architecture modified with g-C₃N₄ has rarely been reported, taking into account the significant challenge to the mineralization of various VOCs.

Herein, we demonstrate a simple hydrothermal method to synthesize MoS₂ nanospheres assemblies with nanosheets and construct the MoS₂@g-C₃N₄ core-shell nanostructures by the ultrasonic adhering approach. By building the core-shell structures, it can integrate different semiconductors into one system and form favorable interface, which can significantly improve the activity including long-term photostability of core and decrease of recombination of photogenerated carriers (Ghosh Chaudhuri and Paria 2012). The crystal structure, morphology, and optical properties of the as prepared MoS₂@g-C₃N₄ core-shell nanospheres were comparatively investigated. As expected, the MoS₂@g-C₃N₄ core-shell nanospheres exhibit enhanced photocatalytic activity comparing with MoS₂ and g-C₃N₄. In addition, the reactive oxide species during the toluene degradation over MoS₂@g-C₃N₄ have been monitored and the proposed mechanisms of toluene degradation have been discussed.

Experimental section

Synthesis of MoS₂@g-C₃N₄ nanospheres

The MoS₂@g-C₃N₄ core-shell nanospheres were fabricated via a two-step approach including the hydrothermal method followed by ultrasonic adhering approach (Pan et al. 2012; Zhang et al. 2015). The synthesis procedure is illustrated in Fig. 1. Firstly, MoS₂ nanospheres were fabricated by the hydrothermal method reported previously with modifications. In a typical case, 0.3 g Na₂MoO₄·2H₂O, 0.6 g NH₂CSNH₂, and poly(vinylpyrrolidone) (PVP) were dissolved in 80 mL deionized water with magnetic stirring for 15 min under the room temperature, followed by transferring into 100 mL Teflon-lined autoclave. After that, the container was placed into an oven and heated at 200 °C for 12 h. After cooling to room temperature naturally, the obtained MoS₂ was collected by centrifugation and dried at 80 °C for 6 h. Secondly, 0.005 g g-C₃N₄, which was obtained from the calcination of melamine at 550 °C for 2 h, was dispersed in 20 mL methanol with ultrasound

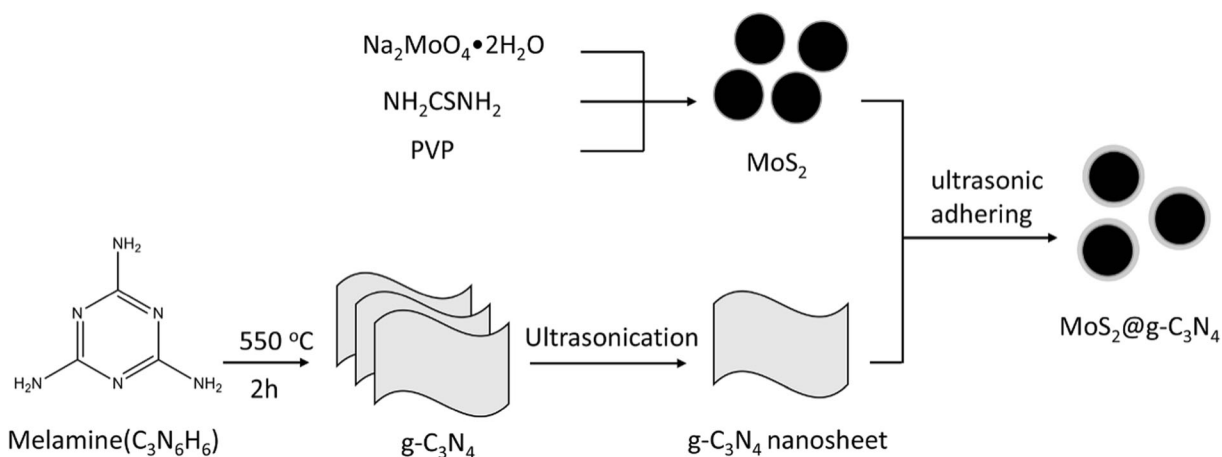


Fig. 1 Schematic diagram of the two-step hydrothermal method approach including the hydrothermal method followed by ultrasonic adhering approach used for the fabrication of $MoS_2@g\text{-}C_3N_4$ core-shell nanospheres

for 100 min. After 0.045 g MoS_2 was added, the mixed solution were stirred in a fume hood until the methanol was volatilized completely. The $MoS_2@g\text{-}C_3N_4$ was obtained by drying at $70\text{ }^\circ\text{C}$ for 8 h.

Characterization

The sample morphology was observed by scanning electron microscope (SEM) (JEOLJSM-6360LV microscope) with an accelerating voltage of 30.0 kV and transmission electron microscopy (TEM, FEI Tecnai G2) at an acceleration voltage of 200 kV, respectively. The crystalline structure of samples were determined by X-ray diffraction (XRD) on Empyrean X-ray diffractometer using $Cu\text{ K}\alpha$ radiation in the range of $10\text{--}80^\circ$. The chemical valences and composition of the sample were measured by an X-ray photoelectron spectroscopy (XPS) (Perkin-Elmer PHI 5600). All the binding energies were referenced to $C\ 1s$ at 285.6 eV. UV-vis diffusive reflectance spectra (DRS) of the as-prepared materials were recorded using UV-vis absorption spectrophotometer (JASCO, UV-550) in the spectral range of 200–800 nm. The FTIR spectra were collected by the FTIR spectrometer (Bruker VERTEX 70-FTIR). To investigate the behavior of the electron-hole pairs, the photoluminescence (PL) characteristics were collected on a Hitachi F-4500 fluorescence spectrophotometer at room temperature with the excitation wavelength of 325 nm. Electron spin resonance (ESR) signals of radicals spin-trapped by spin-trap reagent 5, 5-dimethyl-1-pyrroline-N-oxide (DMPO) were examined with a Bruker A200 spectrometer. The concentration of DMPO was 0.1 mol/L, the volume of reactor was 5 mL, and the

relevant irradiation source was a 500-W high pressure xenon lamp (Shanghai Lansheng Light, China). The parameters for the ESR spectrometer were the following: center field = 3400 G, frequency = 9.46 GHz, microwave power = 20.02 mW.

Photocatalytic activity

Photocatalytic reaction of the materials was evaluated by degradation of toluene under visible light in a home-made in situ quartz infrared reaction cell (Shen et al. 2012). Mixing up the 8-mg catalyst with 35 mg KBr were tableted and settled in the sample holder, followed by sealing the reaction tube. Then, $2\ \mu\text{L}$ of liquid toluene was injected into the reactor by using a microsyringe. Then, after the adsorption-desorption equilibrium in the reactor for 1 h, a 500-W xenon lamp (XQ-500 W) with a 400-nm UV-cutoff filter as the light source was turned on. In situ FTIR spectra during the photocatalytic reaction on $MoS_2@g\text{-}C_3N_4$ nanospheres were recorded using a FTIR spectrometer (Bruker VERTEX 70-FTIR) over accumulative 64 scans with a resolution of 4 cm^{-1} in the range of $4000\text{--}600\text{ cm}^{-1}$.

Results and discussion

Characterization of $MoS_2@g\text{-}C_3N_4$ core-shell nanospheres

The $MoS_2@g\text{-}C_3N_4$ core-shell nanospheres are synthesized by the two-step procedure. Firstly, the MoS_2

nanospheres has been fabricated via the hydrothermal method according to the reported method with miner modification (Zhang et al. 2015). The morphology of the as-prepared MoS₂ has been characterized by the SEM (Fig. 2a). The SEM image clearly confirms that the MoS₂ samples are spherical in shape, with the average diameter of about 166 nm. The MoS₂@g-C₃N₄ core-shell nanospheres are synthesized by a facile ultrasonic adhering approach (Fig. 2b). With the coating of g-C₃N₄ shell, the diameter increases to 250 nm. The thickness of g-C₃N₄ shell can be calculated as about 42 nm by comparing the diameters of MoS₂ and MoS₂@g-C₃N₄. The TEM image in Fig. 2c reveals that the MoS₂ nanospheres are shown to adopt uniform radial orientation and are constructed of ultrathin nanosheets. It needs to point out that the PVP surfactant

absorbed on the surface of MoS₂ could not only prevent the aggregation of MoS₂ nanosheets, but also drive the oriented assembly of the nanosheets into spheres (Zhang et al. 2015). It can clearly see the g-C₃N₄ nanosheets on the surface from the TEM image of MoS₂@g-C₃N₄ (Fig. 2d). The core-shell structure can be conformed from the HRTEM images in Fig. 2e. The existence of MoS₂ nanosheets with radial orientation and amorphous g-C₃N₄ indicated the cover of g-C₃N₄ on the surface of MoS₂ spheres. In addition, the spherical distribution of C and N elements of the EDX mapping (Fig. 2f) can also conform the configuration of core-shell structure. The results of EDX mapping and spectrum (Fig. 2g) reveals that the core-shell nanospheres are composed of Mo, S, C, N, and Si elements (Si signal originates from the underlying substrates in characterization). Moreover,

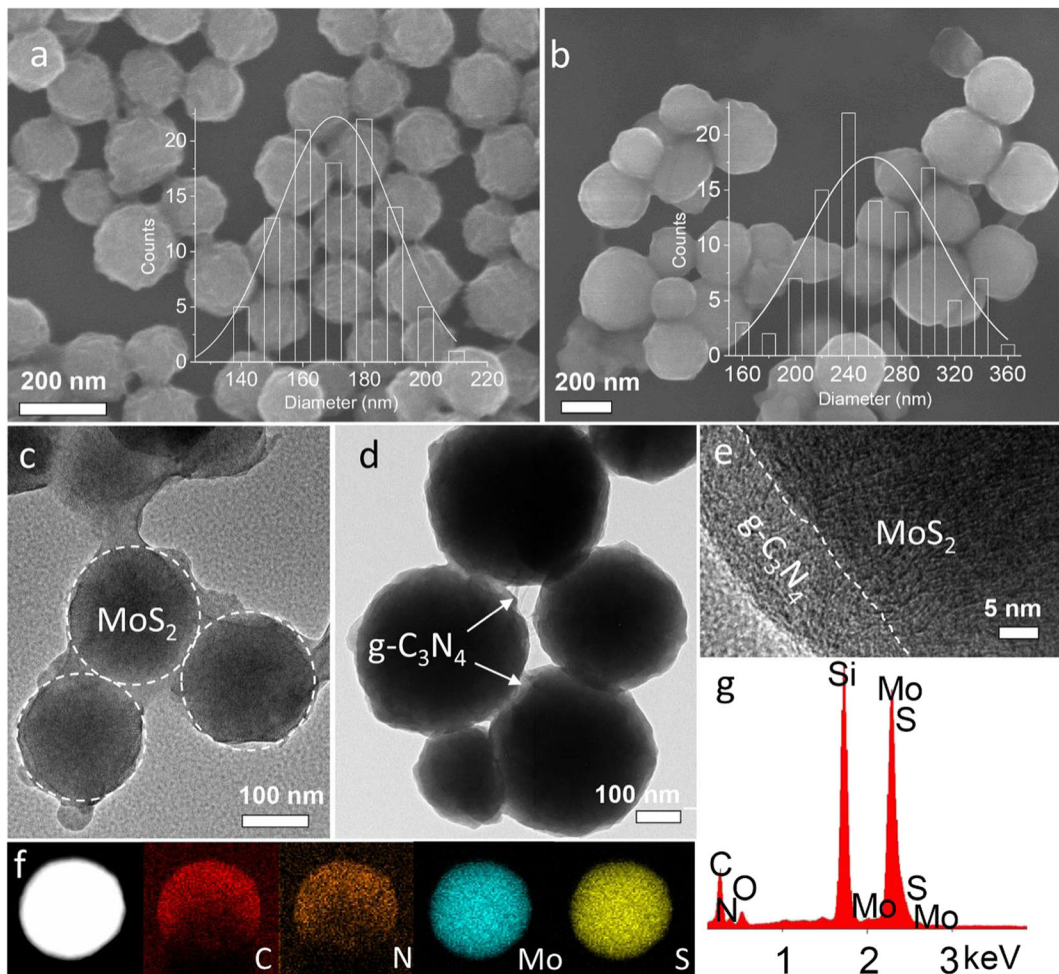


Fig. 2 SEM images of MoS₂ (a) and MoS₂@g-C₃N₄ (b); inset: size distributions of MoS₂ and MoS₂@g-C₃N₄. TEM images of MoS₂ (c) and MoS₂@g-C₃N₄ (d, e). EDX mapping (f) and spectrum (g) of MoS₂@g-C₃N₄

no other elements could be detected within the sensitivity of the apparatuses, indicating high purity of the MoS₂@g-C₃N₄ composites.

The crystallinity and phase purity of the obtained g-C₃N₄, MoS₂ and MoS₂@g-C₃N₄ composites are analyzed by XRD technique (Fig. 3a). The XRD pattern of the MoS₂ samples corresponds to hexagonal MoS₂, which is consistent with the reference values from JCPDS (37-1492) (Zhang et al. 2015). The diffraction peaks at 11.8°, 32.7°, and 57.2° could be ascribed to (002), (100), (101), and (110), respectively. No other peaks could be found. At the same time, the diffraction peaks for the g-C₃N₄ sample shows two diffraction peaks at 27.3° and 13.3°, which result from the (002) and (100) crystal planes, respectively (Dang et al. 2015). It can be seen that all the characteristic diffraction peaks

of MoS₂ can be observed in the composites, indicating that the g-C₃N₄ coated has no impact on the crystalline structure of MoS₂. Meanwhile, the existence of the weak diffraction peak appearing at 27.3° indicates that the g-C₃N₄ has been successfully compounded with MoS₂. However, the diffraction peak of g-C₃N₄ at 13.3° is too close to the peak of MoS₂ at 11.8° to distinguish. In addition, no other significant peaks were detected in the MoS₂@g-C₃N₄ composites, indicating the composites contain g-C₃N₄ and MoS₂ only.

Figure 3b displays the Fourier transform infrared (FTIR) spectra of g-C₃N₄, MoS₂, and MoS₂@g-C₃N₄ core-shell nanospheres. The typical stretching modes revealed a typical molecular structure of g-C₃N₄, which was also supported by the FTIR bands at 1641, 1570, 1461, and 1411 cm⁻¹ corresponding to typical stretching

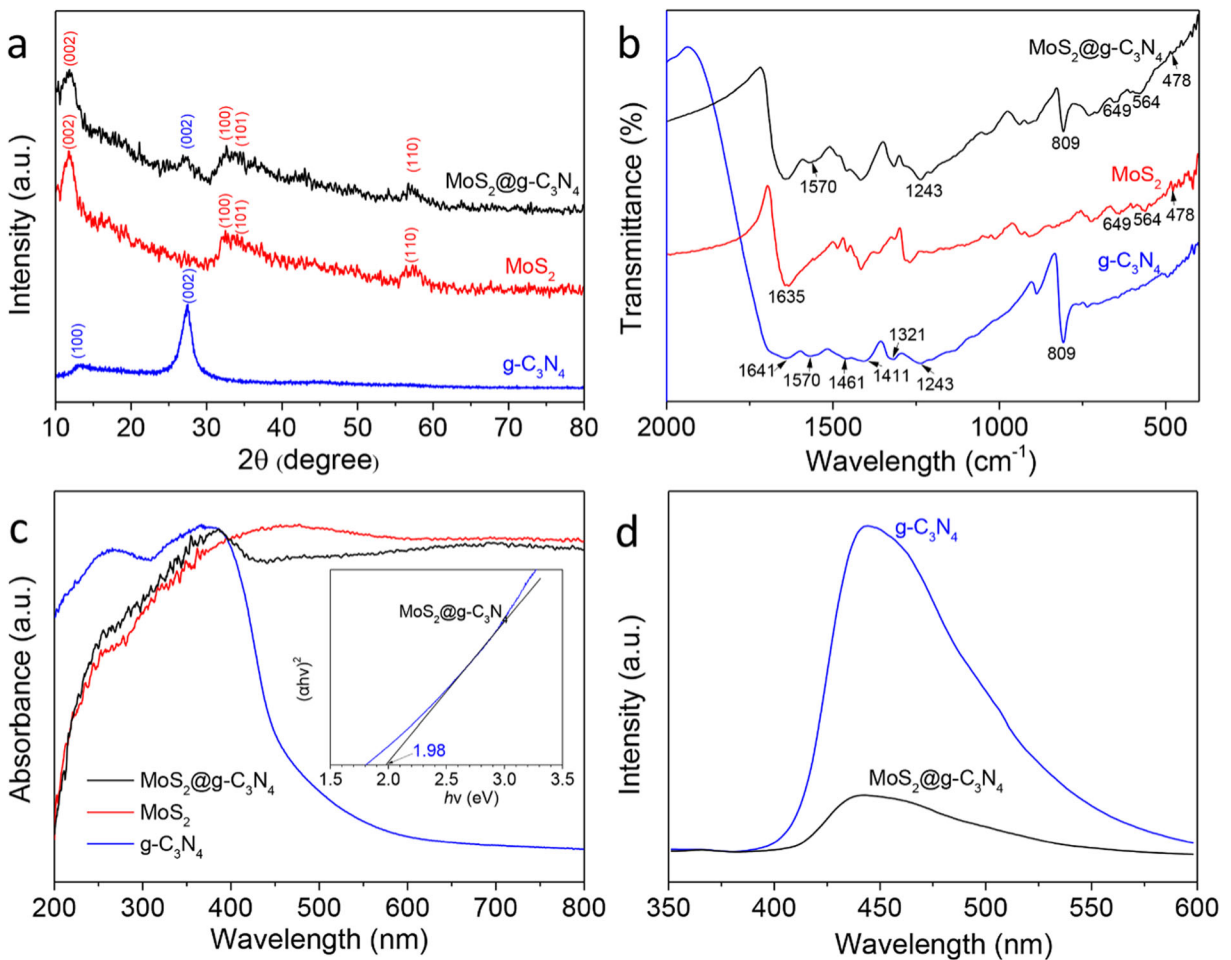


Fig. 3 XRD (a), FTIR (b), and DRS (c) spectra of g-C₃N₄, MoS₂ and MoS₂@g-C₃N₄ (inset: Tauc plots of MoS₂@g-C₃N₄). PL (d) spectra of g-C₃N₄ and MoS₂@g-C₃N₄

vibration modes of heptazine-derived repeating units. In addition, the bands at 1321 and 1243 cm^{-1} of $\text{g-C}_3\text{N}_4$ represent stretching vibration of connected units of C–N(C)–C or C–NH–C, meanwhile, the intense band at 809 cm^{-1} is assigned to the out-of-plane bending vibration of heptazine rings (Liu et al. 2011). For pure MoS_2 , the characteristic peak at 478 cm^{-1} can be observed, which represents the bridging Mo–S bond (Mo–S vibration perpendicular to the basal plane). The peak at 647 cm^{-1} and 562 cm^{-1} can be assigned to S–H vibrations and S–S bonding, respectively (Burman et al. 2016). The typical vibration band of $\text{g-C}_3\text{N}_4$ at 1570, 1243, and 809 cm^{-1} and MoS_2 at 649, 564, and 478 cm^{-1} in the composites indicate the hybridization in $\text{MoS}_2@ \text{g-C}_3\text{N}_4$ nanospheres, while the shift strongly suggests chemical interactions between the core and shell.

The optical properties of as-prepared $\text{g-C}_3\text{N}_4$, MoS_2 , and $\text{MoS}_2@ \text{g-C}_3\text{N}_4$ core-shell nanospheres are shown in Fig. 3c by DRS analysis. As shown in the results, the MoS_2 nanospheres have significant absorption in UV light and visible light regions, which could be deduced from the color of black. However, due to the nature of rapid recombination of photoinduced charges, MoS_2 showed poor photocatalytic activity. The pure $\text{g-C}_3\text{N}_4$ exhibits an absorption edge at about 500 nm due to the intrinsic band gap absorption, which can hardly improve the light absorption in the visible light region. Nevertheless, with MoS_2 coating with $\text{g-C}_3\text{N}_4$, the photoinduced charges transfer between the core and shell could improve the separation of the generated electron-hole pairs. According to the DRS results, the obtained band gap energy (E_g) for $\text{g-C}_3\text{N}_4$ can be calculated as 2.73 eV by Tauc's plots (Pradhan et al. 2013), while the one of pure MoS_2 is 1.67 eV, which is consistent with the previous report (Zou et al. 2015). For the $\text{MoS}_2@ \text{g-C}_3\text{N}_4$ composites, the value of the band gap energy is 1.98 eV. The result indicates that using $\text{MoS}_2@ \text{g-C}_3\text{N}_4$ nanospheres as a core can not only control the morphology of $\text{g-C}_3\text{N}_4$, but also enhance the visible light utilization.

The PL spectra are employed to reveal the transfer and recombination processes of the photogenerated charges during the photocatalysis. It needs to note that the MoS_2 has no photoluminescence property during the room-temperature PL analysis (Li et al. 2015a). Figure 3d presents the PL spectra of $\text{g-C}_3\text{N}_4$ and $\text{MoS}_2@ \text{g-C}_3\text{N}_4$ nanospheres, while that of MoS_2 is absent to avoid misunderstanding. The PL spectrum of

$\text{g-C}_3\text{N}_4$ shows a strong emission centered at around 443 nm, meanwhile, the relative intensity of the peak for $\text{MoS}_2@ \text{g-C}_3\text{N}_4$ nanospheres decreased obviously. It means that the coating of $\text{g-C}_3\text{N}_4$ onto MoS_2 could suppress the recombination of photogenerated charges due to the formation of core-shell nanostructure. The decreasing of recombination of photogenerated charges may enhance the photocatalytic activity of hybrids, which would be conformed following.

To investigate the electronic interactions between MoS_2 and $\text{g-C}_3\text{N}_4$, the XPS analysis has been employed on $\text{MoS}_2@ \text{g-C}_3\text{N}_4$ (Fig. 4). The survey spectra shown in Fig. 4a demonstrate that Mo, S, C, and N elements exist in $\text{MoS}_2@ \text{g-C}_3\text{N}_4$ composites, which is consistent with chemical composition in Fig. 1e. It is proposed that the C 1s peak at around 284.8 eV can be assigned to the signal from carbon contained in the apparatus and is used for calibration. Figure 4b displays the XPS spectra of N 1s. As for the pure $\text{g-C}_3\text{N}_4$, the binding energies at 398.8 and 400.6 eV can be attributed to the presence of C–N–C groups and tertiary nitrogen N–(C)₃ groups (Li et al. 2012). However, both of the N peaks are positively shifted after covering onto the MoS_2 , which indicates that there are strong electronic interactions between the MoS_2 and $\text{g-C}_3\text{N}_4$. In addition, for the pure MoS_2 , the binding characteristic orbital of S 2s, S 2p_{1/2}, S 2p_{3/2}, Mo 3d_{3/2}, and Mo 3d_{5/2} peaks is observed with peak locations at 225, 162, 160.8, 231.1, and 227.9 eV, respectively, which are all consistent with the reported values for MoS_2 (Wang et al. 2014a; Yan et al. 2013). After $\text{g-C}_3\text{N}_4$ covering onto the MoS_2 , S 2s, S 2p_{1/2}, S 2p_{3/2}, Mo 3d_{3/2}, and Mo 3d_{5/2} peaks shift to 225.6, 162.7, 161.4, 232.4, and 228.4 eV, respectively. It is clear that the binding peaks of the core-shell nanospheres shift to a higher binding energies, which also confirms strong electronic interactions involving MoS_2 and $\text{g-C}_3\text{N}_4$ in the core-shell nanospheres (Feng et al. 2015; Zhao et al. 2016). It needs to point out that the weak peak around 168 eV in Fig. 4d can be attributed to the sulfate species from the oxidation of sulfur. The oxidation of sulfur was exacerbated during the evaporation of methanol for the coating of $\text{g-C}_3\text{N}_4$, which caused the increasing of the peak (Li et al. 2016).

Photocatalytic degradation of toluene

The in situ FTIR technique can provide a real-time monitoring of transient events during the photocatalytic degradation of toluene, and the surface-adsorbed species

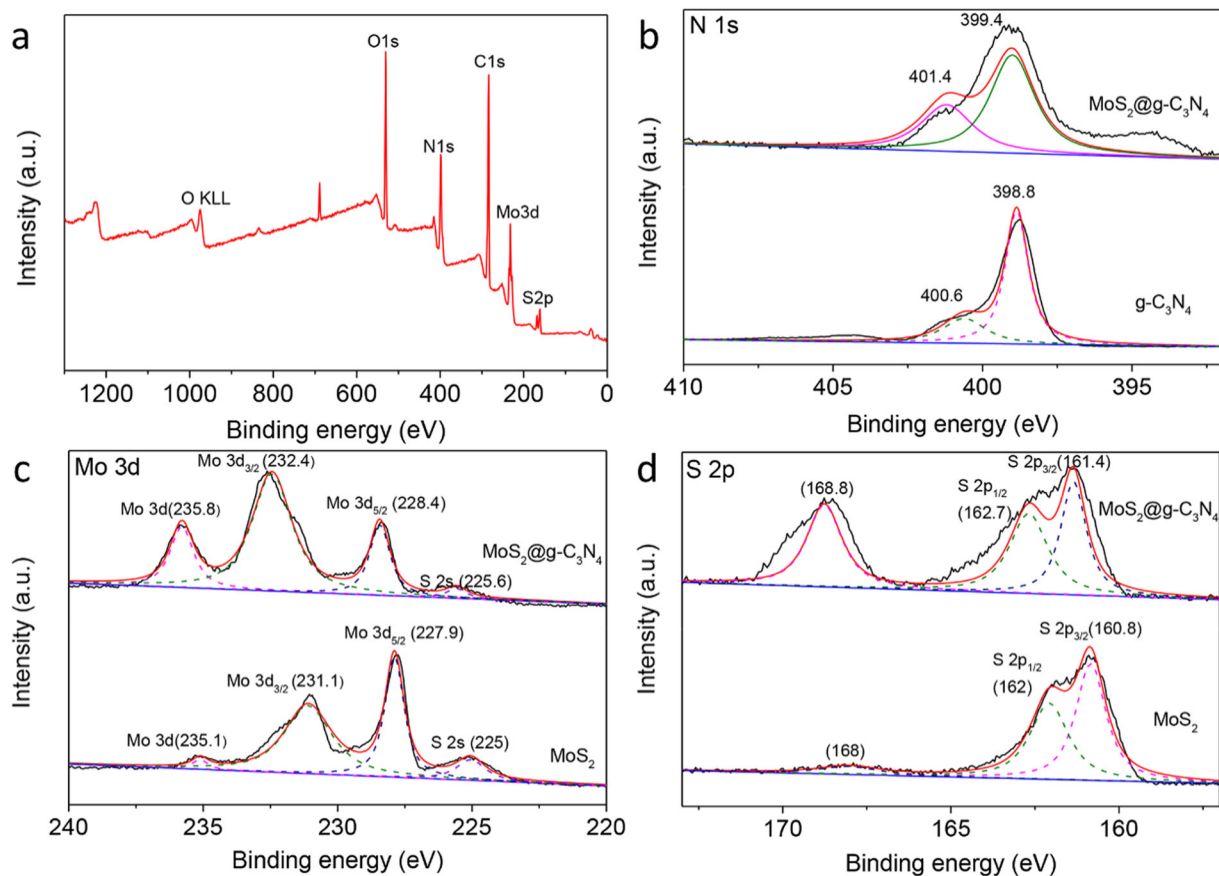


Fig. 4 **a** Survey XPS spectra of $\text{MoS}_2@g\text{-C}_3\text{N}_4$, **b** XPS spectra of N 1s peaks of $\text{MoS}_2@g\text{-C}_3\text{N}_4$ and $g\text{-C}_3\text{N}_4$, **c** Mo 3d and **d** S 2p peaks of $\text{MoS}_2@g\text{-C}_3\text{N}_4$ and MoS_2

of catalysts can be used to analyze the reaction mechanism (Li et al. 2011). A set of FTIR spectra yielded during the photocatalytic degradation of toluene over the $\text{MoS}_2@g\text{-C}_3\text{N}_4$ composites under visible-light irradiation is shown in Fig. 5.

Before visible light irradiation ($t = 0$), the characteristic peaks of toluene at 3076, 3040, 2936, 2881, 1609, and 1499 cm^{-1} can be seen from Fig. 5a. The bands at 3076 and 3040 cm^{-1} are assigned to the C–H stretching mode of the aromatic ring (Liu and Jin 2015), while the bands at 2936 and 2881 cm^{-1} are attributed to the C–H stretching mode of methyl stretching vibration (Maira et al. 2001). In addition, the bands at 1609 and 1499 cm^{-1} are due to the vibrations of aromatic ring. As the irradiation time extended, all the intensity of characteristic peaks of toluene are gradually decreasing. The decreasing peak indicates the degradation of toluene over $\text{MoS}_2@g\text{-C}_3\text{N}_4$ during the photocatalytic reaction. Meanwhile, some new peaks located at 1748, 1732, 1717, 1541, 1506, 1473, 1455, 1396, 1362,

1338, and 1315 cm^{-1} appeared during the photocatalytic reaction proceeding in Fig. 5b. The bands located at 1473 and 1455 cm^{-1} are related to the characteristic peaks of benzyl alcohol and bands at 1362 cm^{-1} and 1338 cm^{-1} attributed to the $\nu(\text{O-H})$ stretching vibration of hydroxy in benzyl alcohol. The bands observed at 1506, 1541, and 1717 cm^{-1} are attributed to the $\nu(\text{C=O})$ stretching vibration of carbonyl compounds in benzaldehyde (Bever et al. 2003; Cao et al. 2000). The 1748, 1732, 1396, and 1315 cm^{-1} are the characteristic peaks of benzoic acid (Domi et al. 2003). In addition, the bands at 2360 and 2340 cm^{-1} indicate the generation of carbon dioxide, while the bands appearing in the 3750–3600 cm^{-1} range are related to hydroxyl groups on the catalyst surface (Fig. 5c). According to the above results and previous reports (Ardizzone et al. 2008; Augugliaro et al. 1999), the intermediate products in the photodegradation of toluene include benzyl alcohol, benzaldehyde, and benzoic acid, followed by mineralizing into carbon dioxide and water finally.

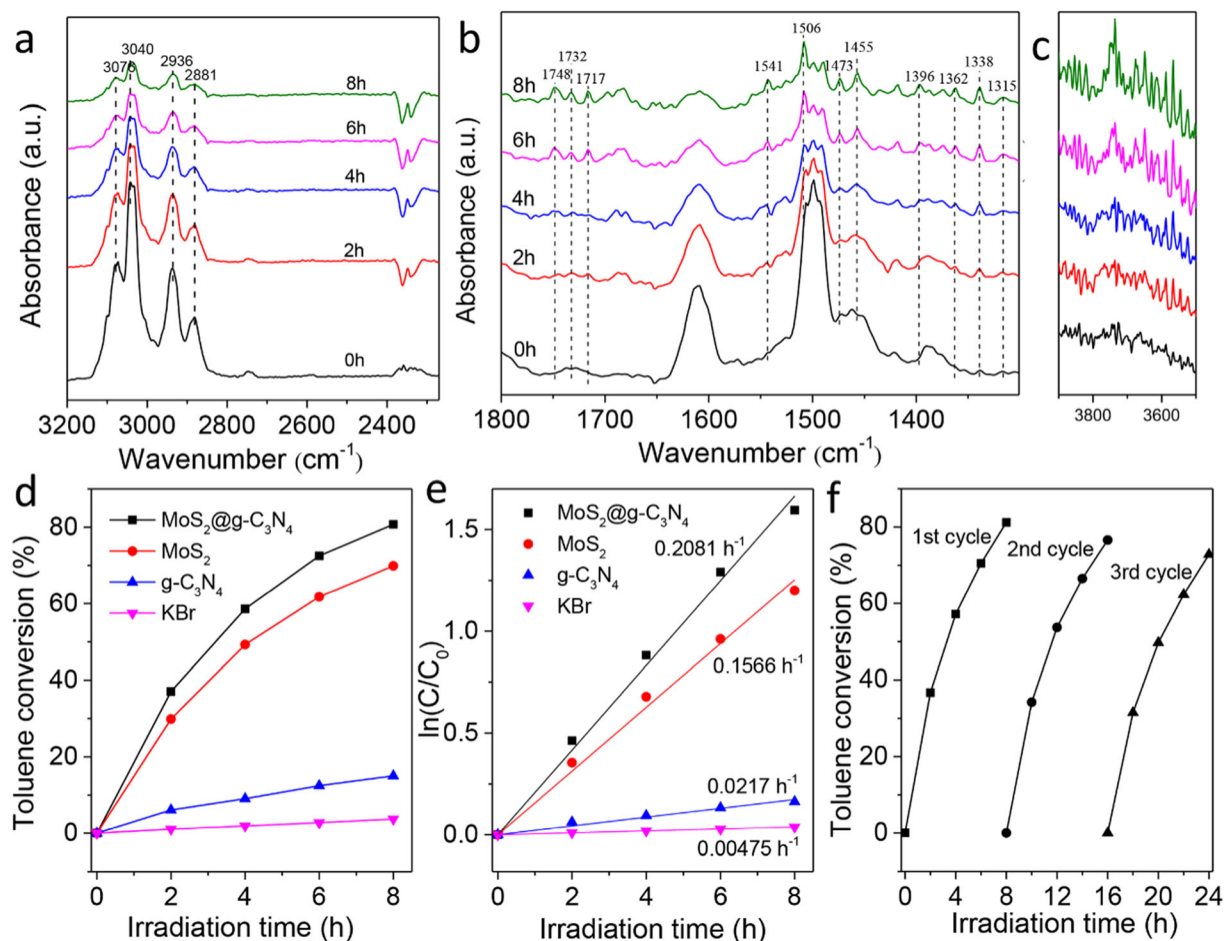


Fig. 5 FTIR spectra in the range of 3200–2300 cm^{-1} (a), 1800–1300 cm^{-1} (b), and 3900–3500 cm^{-1} (c) collected as a function of time for the photodegradation of toluene over the $\text{MoS}_2@\text{g-C}_3\text{N}_4$ under visible light irradiation. **d** Conversion of toluene over the

KBr, $\text{g-C}_3\text{N}_4$, MoS_2 , and $\text{MoS}_2@\text{g-C}_3\text{N}_4$ under visible light irradiation and **e** the related kinetics of toluene degradation by different catalysts. **f** Cycling runs in the photocatalytic degradation of toluene over the $\text{MoS}_2@\text{g-C}_3\text{N}_4$

Figure 5d displays the photocatalytic degradation of toluene over different samples under visible light irradiation. The blank experiment (only with 45 mg KBr) with the toluene conversion of about 3.7% means that the degradation over KBr could be neglected. From the results, it can be seen that the removal efficiency of toluene over $\text{MoS}_2@\text{g-C}_3\text{N}_4$ was as high as 81% after 8 h visible light irradiation time, while there are only 70 and 15% for that of MoS_2 nanospheres and $\text{g-C}_3\text{N}_4$, respectively. The excellent photocatalytic performance of $\text{MoS}_2@\text{g-C}_3\text{N}_4$ nanospheres could be attributed to the fabrication of core-shell nanostructures. Figure 5e shows the related kinetic curves of the different catalysts. The linear transformation of a pseudo-first-order kinetic model was used to fit the degradation data: $-\ln(C_t/C_0) = kt$, where C_t is the concentrations of gaseous

toluene at time t , C_0 is the initial concentration after equilibrium adsorption, and k is the apparent first-order reaction rate constant (Sun et al. 2014). The kinetic constants for $\text{g-C}_3\text{N}_4$ and MoS_2 nanospheres, and $\text{MoS}_2@\text{g-C}_3\text{N}_4$ core-shell nanospheres are 0.0217, 0.1566, and 0.2081 h^{-1} , respectively. With kinetic constant of 9.59 and 1.32 times than that of $\text{g-C}_3\text{N}_4$ and MoS_2 , $\text{MoS}_2@\text{g-C}_3\text{N}_4$ nanospheres show enhanced photocatalytic activity.

In order to examine the stability of the $\text{MoS}_2@\text{g-C}_3\text{N}_4$, the photocatalysis process was repeated three times with the same photocatalyst tablet. After three cycles for the photodegradation of toluene, the $\text{MoS}_2@\text{g-C}_3\text{N}_4$ did not exhibit significant loss of activity, as shown by Fig. 5f, which confirms the excellent stability of the photocatalyst.

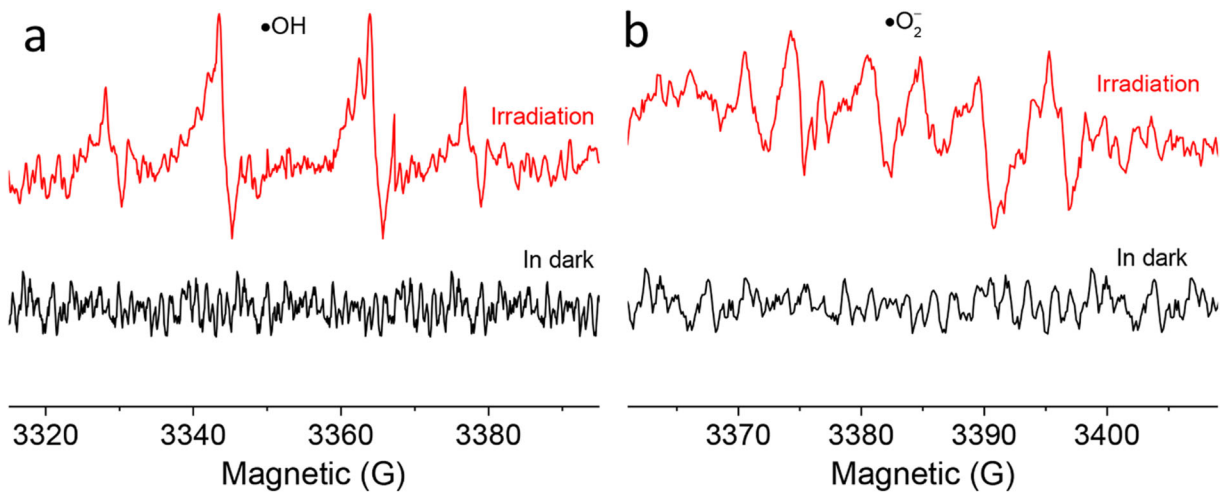
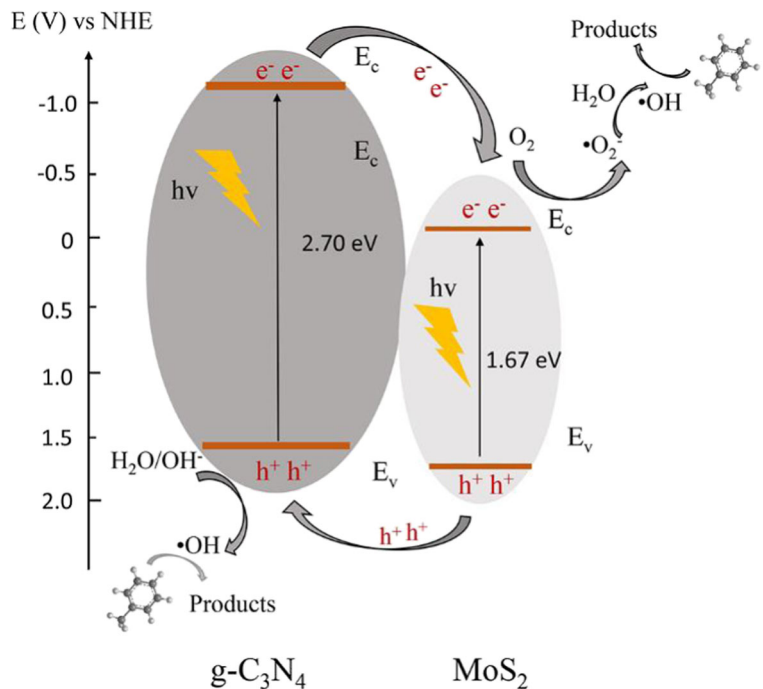


Fig. 6 ESR spectra of MoS₂@g-C₃N₄ suspension solution after 60 s under visible light irradiation: **a** DMPO-·OH formed in irradiated aqueous suspension; **b** DMPO-·O₂⁻ formed in irradiated methanol suspension

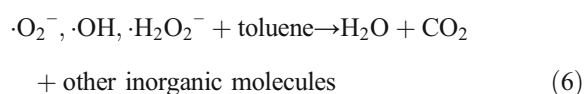
ESR had been employed to confirm the formation of hydroxyl radicals (·OH) and superoxide anion radicals (·O₂⁻) during photocatalytic oxidation. From the ESR spin-trap signals (with DMPO) shown in Fig. 6a, four characteristic peaks with intensity ratio of 1:2:2:1 for the DMPO-·OH were detected with suspensions of the MoS₂@g-C₃N₄ core-shell nanospheres under the visible light illumination. Meanwhile, six characteristic peaks of the DMPO-·O₂⁻ were detected in Fig. 6b. It is

confirmed that spin-trapped DMPO-·OH and DMPO-·O₂⁻ adducts are formed in the process of photocatalytic degradation of toluene during photocatalysis. In contrast, there is no signals of ·OH and ·O₂⁻ that were detected in the dark. The ESR result indicates that the active species ·OH and ·O₂⁻ were produced in the MoS₂@g-C₃N₄ core-shell nanospheres under visible light irradiation, which induced the degradation of organic pollutants.

Fig. 7 Schematic diagram of the photo-induced charge interfacial transfer processes in the MoS₂@g-C₃N₄ after the thermodynamic equilibrium and the associated photochemistry reaction occurring on the surface



Based on the above discussion, a possible photocatalytic mechanism of MoS₂@g-C₃N₄ nanospheres based on the electronic structures, a schematic illustration of interparticle photo-generated charge transfer behavior is shown in Fig. 7. Under the visible light irradiation ($\lambda > 400$ nm), photons can be absorbed by both MoS₂ and g-C₃N₄ to induce h⁺ and e⁻ (Eqs. (1) and (2)). The photogenerated e⁻ migrates to MoS₂ from g-C₃N₄, while the h⁺ transfers through the opposite direction from MoS₂ to g-C₃N₄. Therefore, the transfer of photogenerated charges could improve the separation of them effectively. Some of the photoinduced h⁺ accumulated in g-C₃N₄ could interact with surface-bound H₂O or OH⁻ to produce the ·OH species (Eq. (3)), while the stored e⁻ in the conduction band of MoS₂ can react with the adsorbed O₂ molecules to generate ·O₂⁻ (Eq. (4)). In addition, the OH· radicals are thus likely formed via indirect routes from ·O₂⁻ (Eq. (5)) (Muñoz-Batista et al. 2016). Then, the toluene react with the highly oxidative species, ·OH and ·O₂⁻ and ·H₂O₂⁻, with the intermediate products of benzyl alcohol, benzaldehyde, and benzoic acid, followed by mineralizing into carbon dioxide and water finally (Eq. (6)). According to the above analysis, the relevant reactions at the nanospheres surface can be expressed as follows:



Conclusion

In summary, we have successfully synthesized MoS₂@g-C₃N₄ core-shell nanospheres via a facile hydrothermal and ultrasonic adhering approach using MoS₂ nanospheres as the template. The MoS₂@g-C₃N₄ core-shell nanospheres extended the photo-response range and decreased the recombination rate of the photoinduced electron-hole pairs, therefore exhibited enhanced photocatalytic activity under the visible light irradiation, compared to g-C₃N₄ flake and pure MoS₂ nanospheres. Benefitting from the reactive species such as ·OH and ·O₂⁻ generated during the photocatalytic process, toluene can be mineralized into carbon dioxide and water. The MoS₂@g-C₃N₄ core-shell nanospheres are expected to have promising applications in mineralization of volatile organic pollutants, and further be employed as an efficient visible-light-responsive photocatalyst towards practical application.

Funding information This work was supported financially by the Major Program of the National Natural Science Foundation of China (No. 21590813), the National Natural Science Foundation of China (Nos. 21377015 and 21577012), the Key Project of the National Ministry of Science and Technology (No. 2016YFC0204204), the Program of Introducing Talents of Discipline to Universities (B13012), the Fundamental Research Funds for the Central Universities (DUT16RC(3)095), and the Key Laboratory of Industrial Ecology and Environmental Engineering, China Ministry of Education.

Compliance with ethical standards

Conflict of interest The authors declare that they have no conflict of interest.

References

- Aguero FN, Barbero BP, Gambaro L, Cadús LE (2009) Catalytic combustion of volatile organic compounds in binary mixtures over MnO_x/Al₂O₃ catalyst. *Appl Catal, B* 91:108–112
- Ahmad T, Phul R, Alam P, Lone IH, Shahazad M, Ahmed J, Ahamad T, Alshehri SM (2017) Dielectric, optical and enhanced photocatalytic properties of CuCrO₂ nanoparticles. *RSC Adv* 7:27549–27557
- AlShehri SM, Ahmed J, Ahamada T, Almaswari BM, Khan A (2017a) Efficient photodegradation of methylthioninium chloride dye in aqueous using barium tungstate nanoparticles. *J Nanopart Res* 19:289
- AlShehri SM, Ahmed J, Alzahranian AM, Ahamada T (2017b) Synthesis, characterization, and enhanced photocatalytic

- properties of NiWO₄ nanobricks. *New J Chem* 41:8178–8186
- Ardizzone S, Bianchi CL, Cappelletti G, Naldoni A, Pirola C (2008) Photocatalytic degradation of toluene in the gas phase: relationship between surface species and catalyst features. *Environ Sci Technol* 42:6671–6676
- Atkinson R, Arey J (2003) Atmospheric degradation of volatile organic compounds. *Chem Rev* 103:4605–4638
- Augugliaro V, Coluccia S, Loddo V, Marchese L, Martra G, Palmisano L, Schiavello M (1999) Photocatalytic oxidation of gaseous toluene on anatase TiO₂ catalyst: mechanistic aspects and FT-IR investigation. *Appl Catal*, B 20:15–27
- Barpuzary D, Banik A, Gogoi G, Qureshi M (2015) Noble metal-free counter electrodes utilizing Cu₂ZnSnS₄ loaded with MoS₂ for efficient solar cells based on ZnO nanowires co-sensitized with CuInS₂-CdSe quantum dots. *J Mater Chem A* 3:14378–14388
- Belver C, López-Muñoz MJ, Coronado JM, Soria J (2003) Palladium enhanced resistance to deactivation of titanium dioxide during the photocatalytic oxidation of toluene vapors. *Appl Catal*, B 46:497–509
- Burman D, Ghosh R, Santra S, Guha PK (2016) Highly proton conducting MoS₂/graphene oxide nanocomposite based chemoresistive humidity sensor. *RSC Adv* 6:57424–57433
- Cao L, Gao Z, Suib SL, Obee TN, Hay SO, Freihaut JD (2000) Photocatalytic oxidation of toluene on nanoscale TiO₂ catalysts: studies of deactivation and regeneration. *J Catal* 196: 253–261
- Chen G, Li D, Li F, Fan Y, Zhao H, Luo Y, Yu R, Meng Q (2012) Ball-milling combined calcination synthesis of MoS₂/CdS photocatalysts for high photocatalytic H₂ evolution activity under visible light irradiation. *Appl Catal*, A 443–444:138–144
- Choi MS, Qu D, Lee D, Liu X, Watanabe K, Taniguchi T, Yoo WJ (2014) Lateral MoS₂ p–n junction formed by chemical doping for use in high-performance optoelectronics. *ACS Nano* 8:9332–9340
- Cummins DR, Martinez U, Kappera R, Voiry D, Martinez-Garcia A, Jasinski J, Kelly D, Chhowalla M, Mohite AD, Sunkara MK, Gupta G (2015) Catalytic activity in lithium-treated core-shell MoO_x/MoS₂ nanowires. *J Phys Chem C* 119: 22908–22914
- Dang X, Zhang X, Chen Y, Dong X, Wang G, Ma C, Zhang X, Ma H, Xue M (2015) Preparation of β-Bi₂O₃/g-C₃N₄ nanosheet p–n junction for enhanced photocatalytic ability under visible light illumination. *J Nanopart Res* 17:93
- Domí et al (2003) Silica-supported palladium nanoparticles show remarkable hydrogenation catalytic activity. *J Mol Catal A Chem* 197:185–191
- Feng JX, Ding LX, Ye SH, He XJ, Xu H, Tong YX, Li GR (2015) Co(OH)₂ @PANI hybrid nanosheets with 3D networks as high-performance electrocatalysts for hydrogen evolution reaction. *Adv Mater* 27:7051–7057
- Ghosh Chaudhuri R, Paria S (2012) Core/shell nanoparticles: classes, properties, synthesis mechanisms, characterization, and applications. *Chem Rev* 112:2373–2433
- Gil RR, Ruiz B, Lozano MS, Martín MJ, Fuente E (2014) VOCs removal by adsorption onto activated carbons from biocollagenic wastes of vegetable tanning. *Chem Eng J* 245:80–88
- Hou Y, Zuo F, Dagg A, Feng P (2012) Visible light-driven alpha-Fe₂O₃ nanorod/graphene/BiV_{1-x}Mo_xO₄ core/shell heterojunction array for efficient photoelectrochemical water splitting. *Nano Lett* 12:6464–6473
- Hou Y, Laursen AB, Zhang J, Zhang G, Zhu Y, Wang X, Dahl S, Chorkendorff I (2013) Layered nanojunctions for hydrogen-evolution catalysis. *Angew Chem Int Ed* 52:3621–3625
- Hou H, Gao F, Wang L, Shang M, Yang Z, Zheng J, Yang W (2016) Superior thoroughly mesoporous ternary hybrid photocatalysts of TiO₂/WO₃/g-C₃N₄ nanofibers for visible-light-driven hydrogen evolution. *J Mater Chem A* 4:6276–6281
- Huang J, Hou D, Zhou Y, Zhou W, Li G, Tang Z, Li L, Chen S (2015) MoS₂ nanosheet-coated CoS₂ nanowire arrays on carbon cloth as three-dimensional electrodes for efficient electrocatalytic hydrogen evolution. *J Mater Chem A* 3: 22886–22891
- Hwang H, Kim H, Cho J (2011) MoS₂ nanoplates consisting of disordered graphene-like layers for high rate lithium battery anode materials. *Nano Lett* 11:4826–4830
- Jiang W, Liu Y, Zong R, Li Z, Yao W, Zhu Y (2015) Photocatalytic hydrogen generation on bifunctional ternary heterostructured In₂S₃/MoS₂/CdS composites with high activity and stability under visible light irradiation. *J Mater Chem A* 3:18406–18412
- Kesavan L, Tiruvalam R, Rahim MHA, bin Saiman MI, Enache DI, Jenkins RL, Dimitratos N, Lopez-Sanchez JA, Taylor SH, Knight DW, Kiely CJ, Hutchings GJ (2011) Solvent-free oxidation of primary carbon-hydrogen bonds in toluene using Au-Pd alloy nanoparticles. *Science* 331:195–199
- Kostiainen R (1995) Volatile organic compounds in the indoor air of normal and sick houses. *Atmos Environ* 29:693–702
- Li X, Zou X, Qu Z, Zhao Q, Wang L (2011) Photocatalytic degradation of gaseous toluene over Ag-doping TiO₂ nanotube powder prepared by anodization coupled with impregnation method. *Chemosphere* 83:674–679
- Li J, Shen B, Hong Z, Lin B, Gao B, Chen Y (2012) A facile approach to synthesize novel oxygen-doped g-C₃N₄ with superior visible-light photoreactivity. *Chem Commun* 48: 12017–12019
- Li H, Yu K, Lei X, Guo B, Fu H, Zhu Z (2015a) Hydrothermal synthesis of novel MoS₂/BiVO₄ hetero-nanoflowers with enhanced photocatalytic activity and a mechanism investigation. *J Phys Chem C* 119:22681–22689
- Li X, Hartley G, Ward AJ, Young PA, Masters AF, Maschmeyer T (2015b) Hydrogenated defects in graphitic carbon nitride nanosheets for improved photocatalytic hydrogen evolution. *J Phys Chem C* 119:14938–14946
- Li G, Sun J, Hou W, Jiang S, Huang Y, Geng J (2016) Three-dimensional porous carbon composites containing high sulfur nanoparticle content for high-performance lithium-sulfur batteries. *Nat Commun* 7:10601
- Lin T, Wang J, Guo L, Fu F (2015) Fe₃O₄@MoS₂ core-shell composites: preparation, characterization, and catalytic application. *J Phys Chem C* 119:13658–13664
- Liu B, Jin N (2015) The typical environmental system optimization problems solved by computer software. In: 2015 7th international conference on modelling, identification and control (ICMIC), 18–20 Dec. 2015, pp 1–6
- Liu J, Zhang T, Wang Z, Dawson G, Chen W (2011) Simple pyrolysis of urea into graphitic carbon nitride with recyclable

- adsorption and photocatalytic activity. *J Mater Chem* 21: 14398
- Liu B, Li X, Zhao Q, Ke J, Liu J, Liu S, Tadé M (2015) Photocatalytic degradation of gaseous toluene with multi-phase $\text{Ti}_x\text{Zr}_{1-x}\text{O}_2$ synthesized via co-precipitation route. *J Colloid Interface Sci* 438:1–6
- Lu X, Jin Y, Zhang X, Xu G, Wang D, Lv J, Zheng Z, Wu Y (2016) Controllable synthesis of graphitic C_3N_4 /ultrathin MoS_2 nanosheet hybrid nanostructures with enhanced photocatalytic performance. *Dalton Trans* 45:15406–15414
- Lukowski MA, Daniel AS, Meng F, Forticaux A, Li L, Jin S (2013) Enhanced hydrogen evolution catalysis from chemically exfoliated metallic MoS_2 Nanosheets. *J Am Chem Soc* 135:10274–10277
- Maira AJ, Coronado JM, Augugliaro V, Yeung KL, Conesa JC, Soria J (2001) Fourier transform infrared study of the performance of nanostructured TiO_2 particles for the photocatalytic oxidation of gaseous toluene. *J Catal* 202:413–420
- Malhautier L, Quijano G, Avezac M, Rocher J, Fanlo JL (2014) Kinetic characterization of toluene biodegradation by *Rhodococcus erythropolis*: towards a rationale for microflora enhancement in bioreactors devoted to air treatment. *Chem Eng J* 247:199–204
- Mista W, Kacprzyk R (2008) Decomposition of toluene using non-thermal plasma reactor at room temperature. *Catal Today* 137:345–349
- Muñoz-Batista MJ, Fontelles-Carceller O, Ferrer M, Fernández-García M, Kubacka A (2016) Disinfection capability of $\text{Ag/g-C}_3\text{N}_4$ composite photocatalysts under UV and visible light illumination. *Appl Catal, B* 183:86–95
- Pan C, Xu J, Wang Y, Li D, Zhu Y (2012) Dramatic activity of $\text{C}_3\text{N}_4/\text{BiPO}_4$ Photocatalyst with core/shell structure formed by self-assembly. *Adv Funct Mater* 22:1518–1524
- Parida KM, Sahu N, Tripathi AK, Kamble VS (2010) Gold promoted S,N-doped TiO_2 : an efficient catalyst for CO adsorption and oxidation. *Environ Sci Technol* 44:4155–4160
- Pradhan GK, Padhi DK, Parida KM (2013) Fabrication of $\alpha\text{-Fe}_2\text{O}_3$ nanorod/RGO composite: a novel hybrid photocatalyst for phenol degradation. *ACS Appl Mater Interfaces* 5:9101–9110
- Puértolas B, García-Andújar L, García T, Navarro MV, Mitchell S, Pérez-Ramírez J (2014) Bifunctional Cu/H-ZSM-5 zeolite with hierarchical porosity for hydrocarbon abatement under cold-start conditions. *Appl Catal, B* 154–155:161–170
- Shen Y, Zhao Q, Li X, Yuan D, Hou Y, Liu S (2012) Enhanced visible-light induced degradation of benzene on Mg-ferrite/hematite/PANI nanospheres: in situ FTIR investigation. *J Hazard Mater* 241–242:472–477
- Sun Z, Li X, Guo S, Wang H, Wu Z (2013) One-step synthesis of Cl-doped $\text{Pt(IV)/Bi}_2\text{WO}_6$ with advanced visible-light photocatalytic activity for toluene degradation in air. *J Colloid Interface Sci* 412:31–38
- Sun J, Li X, Zhao Q, Ke J, Zhang D (2014) Novel $\text{V}_2\text{O}_5/\text{BiVO}_4/\text{TiO}_2$ nanocomposites with high visible-light-induced photocatalytic activity for the degradation of toluene. *J Phys Chem C* 118:10113–10121
- Sun J, Li X, Zhao Q, Tade MO, Liu S (2015) Quantum-sized BiVO_4 modified TiO_2 microflower composite heterostructures: efficient production of hydroxyl radicals towards visible light-driven degradation of gaseous toluene. *J Mater Chem A* 3:21655–21663
- Wang Q, Zhang M, Chen C, Ma W, Zhao J (2010) Photocatalytic aerobic oxidation of alcohols on TiO_2 : the acceleration effect of a brønsted acid. *Angew Chem Int Ed* 49:7976–7979
- Wang M, Li G, Xu H, Qian Y, Yang J (2013) Enhanced lithium storage performances of hierarchical hollow MoS_2 nanoparticles assembled from nanosheets. *ACS Appl Mater Interfaces* 5:1003–1008
- Wang PP, Sun H, Ji Y, Li W, Wang X (2014a) Three-dimensional assembly of single-layered MoS_2 . *Adv Mater* 26:964–969
- Wang S, Zhang L, Long C, Li A (2014b) Enhanced adsorption and desorption of VOCs vapor on novel micro-mesoporous polymeric adsorbents. *J Colloid Interface Sci* 428:185–190
- Xiong W, Zhao Q, Li X, Zhang D (2011) One-step synthesis of flower-like Ag/AgCl/BiOCl composite with enhanced visible-light photocatalytic activity. *Catal Commun* 16:229–233
- Yan Y, Xia B, Ge X, Liu Z, Wang J-Y, Wang X (2013) Ultrathin MoS_2 nanoplates with rich active sites as highly efficient catalyst for hydrogen evolution. *ACS Appl Mater Interfaces* 5:12794–12798
- Yu J, Yue L, Liu S, Huang B, Zhang X (2009) Hydrothermal preparation and photocatalytic activity of mesoporous Au-TiO_2 nanocomposite microspheres. *J Colloid Interface Sci* 334:58–64
- Yu L, Lee YH, Ling X, Santos EJJ, Shin YC, Lin Y, Dubey M, Kaxiras E, Kong J, Wang H, Palacios T (2014) Graphene/ MoS_2 hybrid technology for large-scale two-dimensional electronics. *Nano Lett* 14:3055–3063
- Yurdakal S, Palmisano G, Loddo V, Augugliaro V, Palmisano L (2008) Nanostructured rutile TiO_2 for selective photocatalytic oxidation of aromatic alcohols to aldehydes in water. *J Am Chem Soc* 130:1568–1569
- Zhang L, Wu HB, Yan Y, Wang X, Lou XW (2014) Hierarchical MoS_2 microboxes constructed by nanosheets with enhanced electrochemical properties for lithium storage and water splitting. *Energy Environ Sci* 7:3302–3306
- Zhang S, Chowdari BVR, Wen Z, Jin J, Yang J (2015) Constructing highly oriented configuration by few-layer MoS_2 : toward high-performance lithium-ion batteries and hydrogen evolution reactions. *ACS Nano* 9:12464–12472
- Zhao W, Liu Y, Wei Z, Yang S, He H, Sun C (2016) Fabrication of a novel p–n heterojunction photocatalyst $\text{n-BiVO}_4/\text{p-MoS}_2$ with core–shell structure and its excellent visible-light photocatalytic reduction and oxidation activities. *Appl Catal, B* 185:242–252
- Zhou M, Lou XW, Xie Y (2013) Two-dimensional nanosheets for photoelectrochemical water splitting: possibilities and opportunities. *Nano Today* 8:598–618
- Zou X, Dong Y, Li X, Zhao Q, Cui Y, Lu G (2015) Inorganic–organic photocatalyst $\text{BiPO}_4/\text{g-C}_3\text{N}_4$ for efficient removal of gaseous toluene under visible light irradiation. *Catal Commun* 69:109–113